Check for updates

Phase transition, thermal stability, and molecular dynamics of organic–inorganic hybrid perovskite [NH$_3$(CH$_2$)$_6$NH$_3$]CuCl$_4$ crystals†

Moon Young Choi,[a] Seon Ju Lee,[a] Huiyeong Ju[b] and Ae Ran Lim [ID] *[ac]

Organic–inorganic hybrid perovskites have various potential applications in fuel cells and solar cells. In this regard, the physicochemical properties of an organic–inorganic [NH$_3$(CH$_2$)$_6$NH$_3$]CuCl$_4$ crystal was conducted. The crystals had a monoclinic structure with space group $P2_1/n$ and lattice constants $a = 7.2224$ Å, $b = 7.6112$ Å, $c = 23.3315$ Å, $\beta = 91.930°$, and $Z = 4$ at 300 K, and the phase transition temperature (T_C) was determined to be 363 K by X-ray diffraction and differential scanning calorimetry experiments. From the nuclear magnetic resonance experimental results, the changes in the ^{1}H chemical shifts in NH$_3$ and the influence of C1 located close to NH$_3$ in the [NH$_3$(CH$_2$)$_6$NH$_3$] cation near T_C are determined to be large, which implies that the structural change of CuCl$_4$ linked to N–H···Cl is large. The ^{1}H spin–lattice relaxation time ($T_{1\rho}$) in NH$_3$ is shorter than that of CH$_2$, and the ^{13}C $T_{1\rho}$ values for C1 close to NH$_3$ are shorter than those of C2 and C3 due to the influence of the paramagnetic Cu^{2+} ion in square planar geometry CuCl$_4$. The structural mechanism for the phase transition was the change in the N–H···Cl hydrogen bond and was associated with the structural dynamics of the CuCl$_4$ anion.

1. Introduction

Compounds with the general formula [NH$_3$(CH$_2$)$_n$NH$_3$]BX$_4$ ($n = 2, 3, 4, \cdots$, B = divalent metal ion, and X = Cl$^-$, Br$^-$) are known to crystallize as two-dimensional (2D) perovskite-like structures and are generally referred to as organic–inorganic hybrid perovskites.[1–9] Basically, the structure of 2D hybrid perovskite materials consists of organic cations and metal halide layers. The physicochemical properties of organic–inorganic hybrids depend on the organic cations, the inorganic anion coordination geometry of the metal ion, and the halogen ions, which allow the properties of hybrid perovskite to be tailored.[3–5,10–14] The properties of the organic–inorganic hybrid are functions of B and X, and it is important to consider the structural properties of these new materials. The organic cation of the hybrid complex is responsible for structural flexibility and nonlinear optical properties, whereas the inorganic anion is responsible for thermal and mechanical properties.[15,16] Recently, studies on [NH$_3$(CH$_2$)$_n$NH$_3$]BX$_2$X'$_2$ containing different halogen ions were conducted by Abdel-Aal *et al.*[17–19] to improve the optical

properties. When $n \gg 4$, the structural rearrangement due to conformational changes in the chains of long-chain alkylene-diammonium complexes [NH$_3$(CH$_2$)$_n$NH$_3$]BX$_4$ becomes significant.[20–24] As one of them, a group of interest in hybrid materials is perovskite-type layered [NH$_3$(CH$_2$)$_6$NH$_3$]CuCl$_4$ (1,6-hexanediammonium tetrachlorocuprate (II)) containing [NH$_3$(CH$_2$)$_6$NH$_3$] cations and layered CuCl$_4$ anions. In the case of B═Cu, the crystal structures consist of square planar geometry[25] CuCl$_4$$^{2-}$ and organic chains.[16] The CuCl$_4$ anions share corners that extend into infinite sheets separated by alkylene [NH$_3$(CH$_2$)$_6$NH$_3$] groups. The NH$_3$ at both ends of the organic chain is connected by N–H···Cl hydrogen bonds[26,27] with the Cl$^-$ ions of the inorganic layers that stabilize the layered structure, making these materials good candidates as proton conductors,[28] and have potential applications in UV detection.[29,30]

To date, the crystal structure and electrical properties of [NH$_3$(CH$_2$)$_6$NH$_3$]ZnCl$_4$ with B═Zn have been studied by Mostafa and El-Khiyami,[3] while only the optical properties for [NH$_3$(CH$_2$)$_6$NH$_3$]CuCl$_4$ with B═Cu have been reported by Abdel-Aal.[5] Detailed studies on systems where $n = 6$ have not been conducted. Despite the interesting properties of 2D perovskite-like materials, they decompose in humid air and have a similar toxicity to that of Pb.[31–35] Therefore, it is essential to develop a hybrid perovskites that can be replaced with an eco-friendly materials. Recent advances in the development of perovskites have increased the demand for the characterization of their structures and dynamics.

The objective of this study was to investigate the crystal structure, phase transition, and thermodynamic properties of

[a]Graduate School of Carbon Convergence Engineering, Jeonju University, Jeonju 55069, South Korea

[b]Korea Basic Science Institute, Seoul Western Center, Seoul 03759, South Korea

[c]Department of Science Education, Jeonju University, Jeonju 55069, South Korea. E-mail: aeranlim@hanmail.net; arlim@jj.ac.kr

† Electronic supplementary information (ESI) available: XRD data, bond distances and angles, and hydrogen-bond geometries of the crystal structure. CCDC 2170927. For ESI and crystallographic data in CIF or other electronic format see https://doi.org/10.1039/d2ra02975h

$[NH_3(CH_2)_6NH_3]CuCl_4$. We also discuss the roles of cations in single-crystal $[NH_3(CH_2)_6NH_3]CuCl_4$ near the phase transition temperature (T_C). Chemical shifts and spin–lattice relaxation times ($T_{1\rho}$) were studied using ^1H magic angle spinning (MAS) nuclear magnetic resonance (NMR) and ^{13}C MAS NMR to understand the structural environment and molecular motions of the organic chain. These results help explain the physical, chemical, and thermal properties, as well as structural dynamics based on the phase transition mechanism for the practical application of $[NH_3(CH_2)_6NH_3]CuCl_4$ crystals.

2.   Experimental

$[NH_3(CH_2)_6NH_3]CuCl_4$ single crystals were grown from saturated aqueous solutions containing stoichiometric quantities of hexane-diammonium dichloride ($NH_2(CH_2)_6NH_2 \cdot 2HCl$, Sigma-Aldrich, 99%) and copper chloride ($CuCl_2$, Sigma-Aldrich, 99%) in the molar ratio of 1 : 1 at 300 K. The mixture was stirred and heated to obtain a homogeneous solution. The resulting solution was filtered and single crystal were obtained by slow evaporation. Light brown single crystals of approximately 4 × 3 × 1 mm were grown at constant temperature for approximately 3 weeks.

Fourier transform infrared (FT-IR) spectra were measured between 4000 and 500 cm^{-1} on a PerkinElmer (L1600300) spectrometer using a compressed KBr pellet.

The lattice parameters at various temperatures were determined by single-crystal X-ray diffraction (XRD) at the Seoul Western Center of the Korea Basic Science Institute (KBSI). A colorless crystal block was picked up with paratone oil and mounted on a Bruker D8 Venture PHOTON III M14 diffractometer equipped with a graphite-monochromated Mo-Kα ($\lambda = 0.71073$ Å) radiation source and a nitrogen cold stream (−50 °C). Data was collected and integrated using SMART APEX3 (Bruker, 2016) and SAINT (Bruker, 2016). The absorption was corrected by a multi-scan method implemented in SADABS. The structure was solved using direct methods and refined by full-matrix least-squares on F^2 using SHELXTL. All non-hydrogen atoms were refined anisotropically, and the hydrogen atoms were added to their geometrically ideal positions. Additionally the powder XRD patterns of the $[NH_3(CH_2)_6NH_3]CuCl_4$ crystals were measured at several temperatures using an XRD system with a Mo-Kα radiation source. Experiments were conducted using the method described here.[35]

Differential scanning calorimetry (DSC) thermogram were observed using a DSC (25, TA Instruments) at heating and cooling speeds of 10 °C min^{-1} between 200 and 500 K under a flow of dry nitrogen gas.

Thermogravimetric analysis (TGA) was measured on a thermogravimetric analyzer with heating speed of 10 °C min^{-1} between 300 and 873 K under N_2 gas. In addition, optical observations between 300 and 680 K were made using a Carl Zeiss optical polarized microscope.

NMR spectra of $[NH_3(CH_2)_6NH_3]CuCl_4$ crystals were obtained using a Bruker 400 MHz Avance II + solid-state NMR spectrometer at the same facility, KBSI. The Larmor frequency for ^1H MAS NMR was $\omega_o/2\pi = 400.13$ MHz and that for ^{13}C MAS

NMR was $\omega_o/2\pi = 100.61$ MHz. The MAS rate was set at a speed of 10 kHz to minimize sideband, and tetramethylsilane (TMS) was used as a basic materials to accurately measure the NMR chemical shift. The $T_{1\rho}$ values were obtained from the spectra measured using a $\pi/2 - \tau$ pulse followed by a spin-lock pulse of duration τ, and the $\pi/2$ pulse widths for ^1H and ^{13}C were measured using the method described here.[36]

3.   Results and discussion

3.1   FT-IR spectra

The FT-IR spectra at room temperature were obtained between 4000 and 500 cm^{-1}, and their result is shown in Fig. 1. The strong band at around 3116 cm^{-1} was assigned to the C–H mode, and the band at 2928 cm^{-1} was expected when N–H⋯Cl hydrogen bonds are formed. The peaks at 1576 and 1480 cm^{-1} corresponded to asymmetric NH_3 deformation and symmetric NH_3 deformation, respectively. Bands near 1102 and 921 cm^{-1} were defined to the C–N and C–C modes, respectively. These results are consistent with those reported by Abdel-Aal et al.[5]

3.2   Crystal structure

Single-crystal XRD results for $[NH_3(CH_2)_6NH_3]CuCl_4$ crystals were obtained at 300 K. The hybrid was found to have crystallized as a monoclinic system with a space group $P2_1/n$ and had lattice constants $a = 7.2224$ Å, $b = 7.6112$ Å, $c = 23.3315$ Å, $\beta = 91.930°$, and $Z = 4$. Table 1 lists single-crystal XRD and refinement data of the $[NH_3(CH_2)_6NH_3]CuCl_4$ crystal, and Fig. 2 shows its structure. The Cu atom is coordinated by four Cl atoms, forming a square planar geometry of $CuCl_4$. The hydrogen atoms of each formula unit are able to form hydrogen bonds N–H⋯Cl. The atomic numbering scheme and thermal ellipsoids for the H atoms are shown in Fig. 3, and their bond lengths and angles are summarized in Table 2. The asymmetric unit contains two half $[NH_3(CH_2)_6NH_3]$ and one $CuCl_4$. The detailed results of the crystal structure are shown in ESI.†
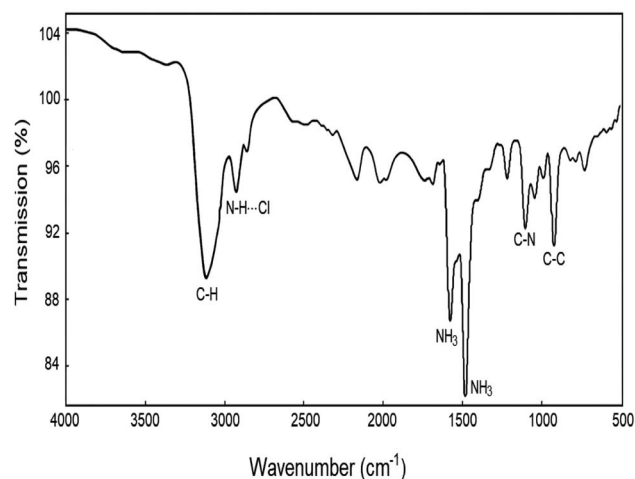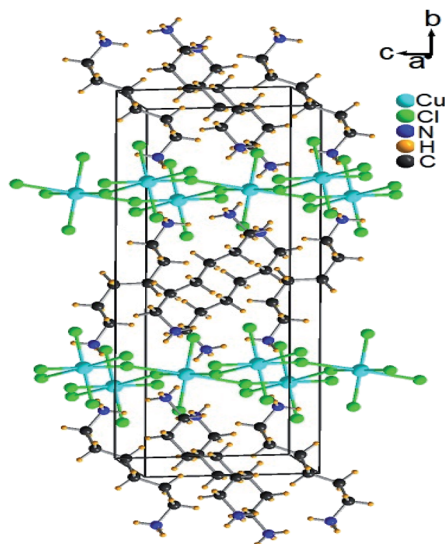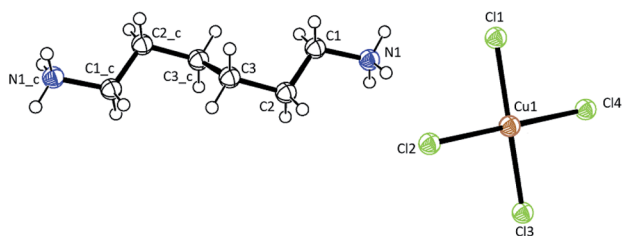

Fig. 1   IR spectrum of $[NH_3(CH_2)_6NH_3]CuCl_4$ between 4000 and 500 cm^{-1} at room temperature.

Table 1 Crystal data and structure refinement for [NH$_3$(CH$_2$)$_6$NH$_3$]CuCl$_4$ at 300 K. The full data are available in the CIF files

Chemical formula	C$_6$H$_{18}$N$_2$CuCl$_4$
Weight	323.56
Crystal system	Monoclinic
Space group	$P2_1/n$
T (K)	300
a (Å)	7.2224
b (Å)	7.6112
c (Å)	23.3315
β (°)	91.930
Z	4
V (Å^3)	1281.83
Radiation type	Mo-Kα
Wavelength (Å)	0.71073
Reflections collected	22 737
Independent reflections	3182 (R_{int} = 0.0568)
Goodness-of-fit on F^2	1.071
Final R indices [I > 2sigma(I)]	R_1 = 0.0510, wR_2 = 0.1214
R indices (all data)	R_1 = 0.0793, wR_2 = 0.1407

Table 2 Bond-lengths (Å) and Bond-angles (°) at 300 K[a]

Bond-length (Å) and Bond-angle (°)	
Cl(1)–Cu(1)	2.2905 (12)
Cl(2)–Cu(1)	2.3093 (12)
Cl(3)–Cu(1)	2.2891 (12)
Cl(4)–Cu(1)	2.3031 (12)
N(1)–C(1)	1.495 (7)
C(1)–C(2)	1.445 (8)
C(2)–C(3)	1.536 (9)
C(3)–C(3)_c	1.517 (13)
C(3)_c–C(2)_c	1.508 (8)
C(2)_c–C(1)_c	1.481 (8)
Cl(2)–Cu(1)–Cl(3)	90.27 (4)
Cl(2)–Cu(1)–Cl(4)	179.71 (5)
Cl(3)–Cu(1)–Cl(4)	89.51 (4)
Cl(2)–Cu(1)–Cl(1)	89.74 (5)
Cl(3)–Cu(1)–Cl(1)	179.83 (5)
Cl(1)–Cu(1)–Cl(4)	90.47 (4)

[a] Symmetry operations: (a) $-x + 3/2, y - 1/2, -z + 1/2$; (b) $-x + 1/2, y + 1/2, -z + 1/2$.

Fig. 2 Crystal structure of [NH$_3$(CH$_2$)$_6$NH$_3$]CuCl$_4$ at 300 K [A.R. Lim CCDC 2170927].

Further, XRD powder patterns of the [NH$_3$(CH$_2$)$_6$NH$_3$]CuCl$_4$ crystal were obtained at different temperatures during heating, and the results are shown in Fig. 4. The XRD patterns at 300 and 350 K were identical, and the XRD patterns at temperatures above 370 K were the same as those at 380 and 400 K. At 360 K (red), it can be seen that the phase at 350 K and the phase at 370 K coexist. The XRD pattern taken at 360 K showed a clear change in symmetry associated with a phase transition. The final pattern (olive) is depicted after being cooled down to room temperature (300 K). It shows that the crystal undergoes an reversible phase transition as is clearly seen by the differences of the XRD powder pattern obtained at 300 K before heating and 300 K after cooling.

3.3 Phase transition

Fig. 5 shows the results of heating and cooling at a speed of 10 °C min^{-1} for the DSC experiment on [NH$_3$(CH$_2$)$_6$NH$_3$]CuCl$_4$ crystals. As a result of heating, an endothermic peak was observed at 363 K, and an exothermic peak due to cooling was

Fig. 3 Thermal ellipsoid plot (50% probability) for structure of [NH$_3$(-CH$_2$)$_6$NH$_3$]CuCl$_4$.

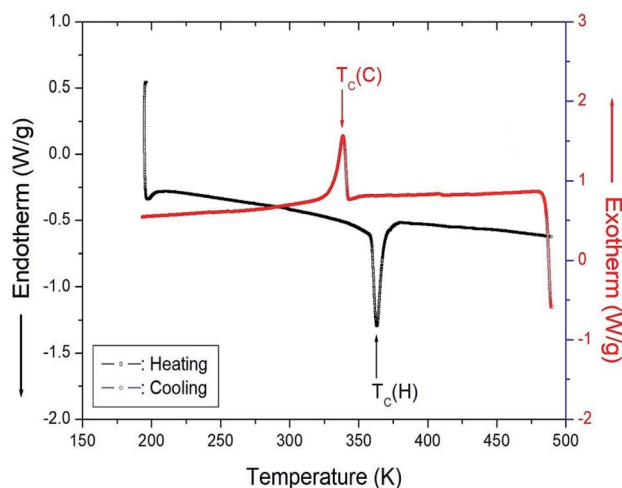**Fig. 4** Powder X-ray diffraction patterns of [NH$_3$(CH$_2$)$_6$NH$_3$]CuCl$_4$ at different temperatures.

Fig. 5 Differential scanning calorimetry (DSC) curves for heating and cooling in [NH$_3$(CH$_2$)$_6$NH$_3$]CuCl$_4$.

observed at 338 K. The temperature of 363 K shown in the DSC curve is the same as the change at 360 K, as shown in the XRD results. This temperature was expressed as the phase transition temperature T_C (H) (=363 K) and T_C (C) (=338 K) according to heating and cooling, respectively.

3.4 Thermal properties

The TGA and differential thermal analysis (DTA) experimental results were measured at the same heating rate used in the DSC experiment to understand the thermal properties, and the results are shown in Fig. 6. Mass loss began at approximately 507 K, which represents the onset of partial thermal decomposition. The molecular weight of the [NH$_3$(CH$_2$)$_6$NH$_3$]CuCl$_4$ decreased with increasing temperature. From the total molecular weight (Mw = 323.57 mg), the amount of residue was determined using eqn (1) and (2).[37]
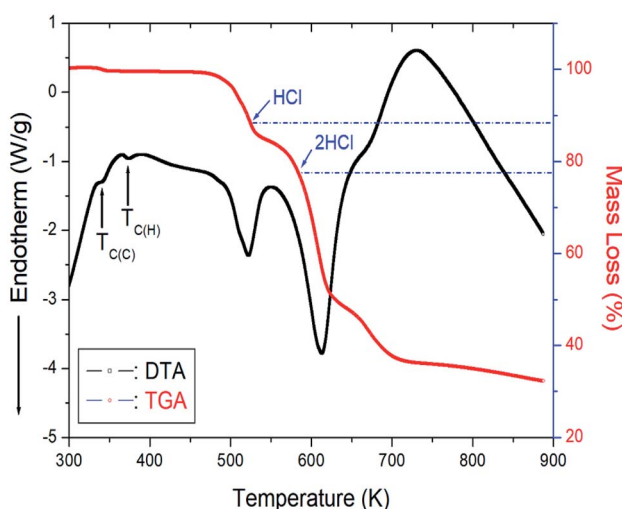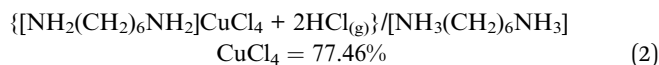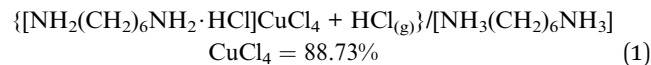
$$\{[NH_2(CH_2)_6NH_2 \cdot HCl]CuCl_4 + HCl_{(g)}\}/[NH_3(CH_2)_6NH_3]$$
$$CuCl_4 = 88.73\% \quad (1)$$

$$\{[NH_2(CH_2)_6NH_2]CuCl_4 + 2HCl_{(g)}\}/[NH_3(CH_2)_6NH_3]$$
$$CuCl_4 = 77.46\% \quad (2)$$

The losses of 11% and 23% calculated from the molecular weight were affected by the decomposition of HCl and 2HCl, respectively, and the temperature of HCl and 2HCl loss obtained by TGA experiment were 527 and 584 K. Near 900 K, the weight loss of 70% occurred. The mass sharply decreased between 510 and 600 K, with a corresponding mass loss of 50% near 650 K.

On the other hand, to support the DSC and TGA results, the morphology of single crystals with changing temperature is observed using an optical polarizing microscopy experiment. The crystal was light brown at room temperature. As the temperature increased, the crystal turned brown, and the crystal was dark brown above 490 K. Finally, the surface of the single crystal was slightly melted near 540 K. However, the two small endothermic peaks near 345 and 370 K in the DTA curve were assigned to the phase transition temperature detected during cooling and heating, respectively, in the DSC results.

3.5 ^{1}H MAS NMR spectrum

The ^{1}H MAS NMR spectra of [NH$_3$(CH$_2$)$_6$NH$_3$]CuCl$_4$ crystals were measured while increasing the temperature, and the results of *in situ* ^{1}H chemical shifts between 180 and 410 K are shown in Fig. 7. At low temperatures, only one resonance signal for ^{1}H of NH$_3$ was recorded and the line width for ^{1}H of CH$_2$ was too broad to be measured. However, as the temperature increased, the NMR spectrum showed two resonance lines for NH$_3$ and CH$_2$. At 300 K, the ^{1}H chemical shifts for NH$_3$ and CH$_2$ were 12.14 and 2.24 ppm, respectively. The spinning sidebands

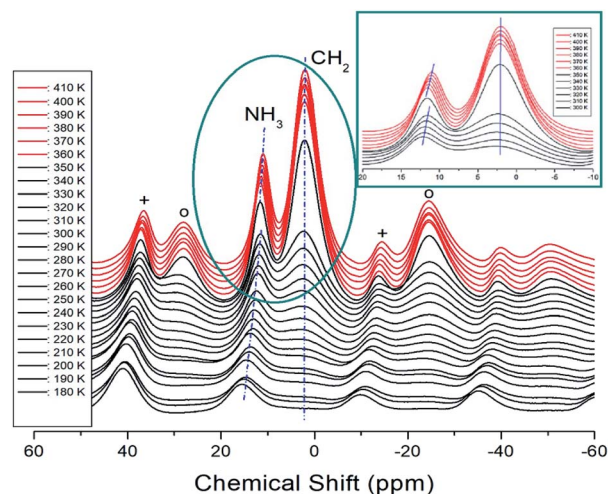Fig. 6 Thermogravimetric analysis (TGA) and differential thermal analysis (DTA) curves of [NH$_3$(CH$_2$)$_6$NH$_3$]CuCl$_4$.

Fig. 7 MAS ^{1}H NMR spectrum of [NH$_3$(CH$_2$)$_6$NH$_3$]CuCl$_4$ above (red region) and below T_C (black region) according to the heating. The spinning sidebands are indicated by crosses and open circles (inset: enlarged ^{1}H NMR spectrum near T_C).

for NH_3 and CH_2 are marked with pluses and open circles, respectively. The chemical shifts at temperatures below T_C (=363 K) are represented in black, and those at temperatures above T_C are represented in red. In the case of heating, the chemical shifts change at approximately 360 K in the ^1H NMR spectrum. A detailed picture is shown in the inset of Fig. 7, where the ^1H chemical shifts of CH_2, indicated by dotted lines, are almost temperature-independent over a wide temperature range, whereas those of NH_3 are discontinuous and vary significantly near T_C. In addition, the number of protons related to NH_3 and CH_2 in the $[NH_3(CH_2)_6NH_3]$ cation were 6 and 12, respectively, and the intensity of the ^1H resonance peak was related to the number of protons. The large change in the ^1H chemical shift of NH_3 of the organic group near T_C is due to the change in N–H⋯Cl hydrogen connected by the inorganic group.

3.6 ^{13}C MAS NMR spectrum

The ^{13}C chemical shifts for the *in situ* MAS NMR spectra for heating and cooling are shown in Fig. 8 and 9, respectively. The TMS reference signal for ^{13}C at 300 K was recorded at 38.3 ppm, and this value was taken as the standard for the ^{13}C chemical shift. In the $[NH_3(CH_2)_6NH_3]$ cation, CH_2 close to NH_3 at both ends of the organic chain was designated C1, CH_2 at the middle of 6 CH_2 chains was designated C3, and CH_2 between C1 and C3 was designated C2, as shown in the inset of Fig. 8. Fig. 8 shows the ^{13}C MAS NMR spectra measured during heating. At low temperatures, 4–5 resonance lines were reduced to three resonance lines near T_C. Here, the spectrum below the phase transition temperature of 360 K is shown in black, and the spectrum above 360 K is shown in red. In addition, the chemical shifts of C1 changed rapidly with temperature compared to those of C2 and C3. These results show that C1, which is close to N, has the greatest change with temperature. On the other hand, in the case of cooling, the results of the ^{13}C MAS NMR spectrum are presented in Fig. 9; it shows that the spectrum changes near 350 K, which is slightly different from the 338 K obtained in the DSC curve. Here, the phase transition temperature is depicted by the
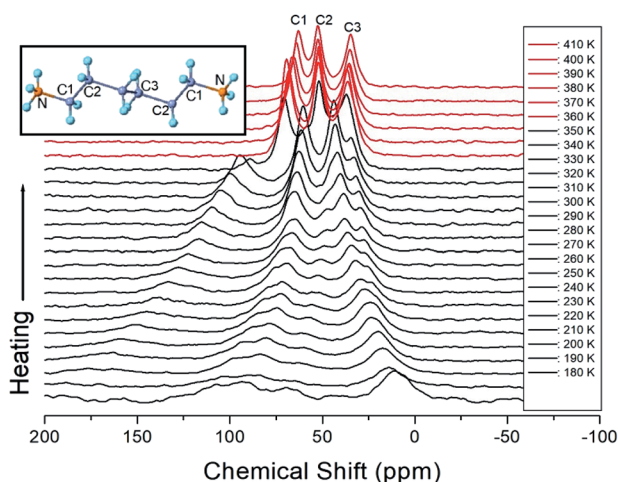

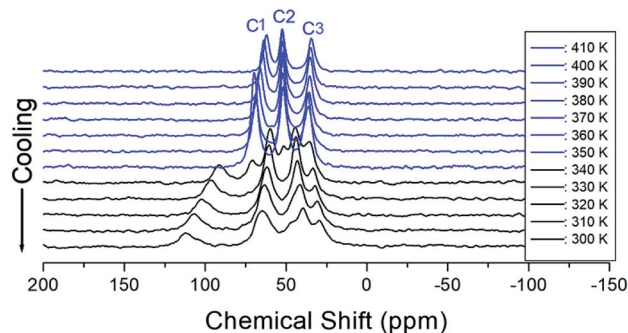**Fig. 9** MAS ^{13}C NMR spectrum of $[NH_3(CH_2)_6NH_3]CuCl_4$ above (blue region) and below T_C (black region) according to the cooling.

blue line above T_C, and the black line below T_C is the boundary. The chemical shifts were the same at all temperatures during heating and cooling, but only the phase transition temperature was different. At 400 K, the ^{13}C chemical shifts were recorded at 118.46, 50.94, and 27.19 ppm for C1, C2, and C3, respectively. From this result, the surrounding environments of all the ^{13}C ions changed according to the temperature. Similar to the result of H, it was found that the chemical shift of C1 close to N changed the most. As determined from this result, C1 is most closely connected with the N–H⋯Cl bond; thus, the change in C1 is thought to be indirectly related to the change in square planar geometry $CuCl_4$.

For the MAS NMR probe, the difference between the set temperature and sample temperature inside the probe was previously reported by Guan and Stark.[38] The equation for fast MAS probe is

$$T_S(f) = 0.98 \ T_O + 3.79 \ (°C) \exp(\omega_r/19.6 \ kHz) - 3.49 \ (°C) \quad (3)$$

where T_O is the set temperature and ω_r is the MAS spinning rate. For instance, a set temperature of 360 K for a sample spinning rate of 10 kHz corresponds to 361 K in the fast MAS probe. The difference in temperature shown by DSC and NMR is very small for this fast MAS probe.

3.7 ^1H and ^{13}C spin–lattice relaxation times

The ^1H and ^{13}C MAS NMR spectra were measured with varying delay times at each given temperature, and the plot of spectral intensities *versus* delay times was found to follow a mono-exponential function. The decay rate of the magnetization is characterized by the spin–lattice relaxation time ($T_{1\rho}$) as[39–41]

$$P_{H(C)}(\tau) = P_{H(C)}(0) \exp(-\tau/T_{1\rho}) \quad (4)$$

where $P_{H(C)}(\tau)$ and $P_{H(C)}(0)$ are the signal intensities for the proton (carbon) at time τ and $\tau = 0$, respectively. The ^1H $T_{1\rho}$ values for NH_3 and CH_2 were determined from the slope of the logarithm of intensities *versus* delay time plots at several temperatures. The ^1H $T_{1\rho}$ results are represented in Fig. 10 as a function of the 1000/temperature. The ^1H $T_{1\rho}$ values are nearly independent of temperature on the order of 10 ms. Here, the ^1H $T_{1\rho}$ values in NH_3 are shorter than those in CH_2. In addition, the
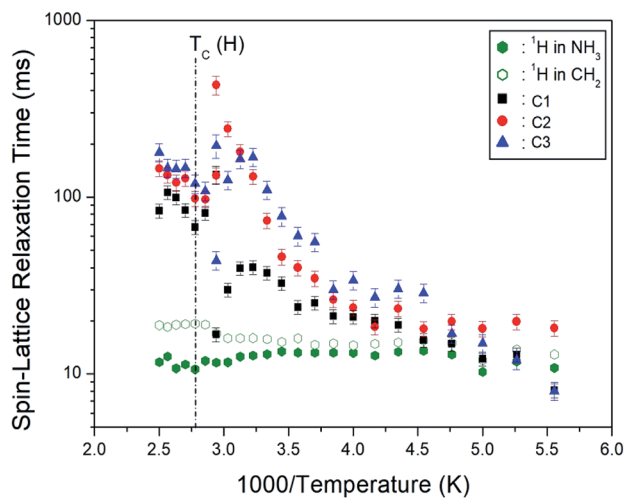

Fig. 8 MAS ^{13}C NMR spectrum of $[NH_3(CH_2)_6NH_3]CuCl_4$ above (red region) and below T_C (black region) according to the heating.

Fig. 10 Temperature dependences of ^1H and ^{13}C NMR spin–lattice relaxation times $T_{1\rho}$ in $[NH_3(CH_2)_6NH_3]CuCl_4$.

^{13}C $T_{1\rho}$ values for C1, C2, and C3 were obtained from the slope of their ^{13}C recovery traces. The ^{13}C $T_{1\rho}$ values increase rapidly from 10 to 400 ms. The behavior of $T_{1\rho}$ for random motions with correlation time τ_C is described by fast motion with increasing temperature. ^1H and ^{13}C $T_{1\rho}$ values at low and high temperatures were represented in the fast motion regime, where $\omega_1\tau_C \ll 1$ and $T_{1\rho}^{-1} \propto \exp(E_a/k_BT)$.[39] The reason the $T_{1\rho}$ value of C1 is less than the $T_{1\rho}$ values of C2 and C3 is that the C–C bond length represented by C2 and C3 is 1.526 Å, and the C–N bond length represented by C1 is 1.495 Å, which is shorter than C2 and C3. The $T_{1\rho}$ value is proportional to the bond length, r^6.[39] In addition, the $T_{1\rho}$ of C1 located close to the paramagnetic Cu^{2+} ion is shorter than the $T_{1\rho}$ values of C2 and C3 located far from Cu^{2+}, as expected. That is, $T_{1\rho}$ is related to the magnetic moment of the paramagnetic ion; it is inversely proportional to the square of this value.

4. Conclusions

To understand the structural, thermodynamic, and physico-chemical properties of the hybrid perovskite $[NH_3(CH_2)_6NH_3]$ $CuCl_4$ crystal, XRD, DSC, TGA, and NMR experiments were performed. First, the $[NH_3(CH_2)_6NH_3]CuCl_4$ crystals at 300 K belong to a monoclinic system with a space group $P2_1/n$, and the lattice constants are $a = 7.2224$ Å, $b = 7.6112$ Å, $c = 23.3315$ Å, $\beta = 91.930°$, and $Z = 4$ (CCDC 2170927). The phase transition temperature was determined to be $T_C = 363$ K based on the DSC results and XRD powder patterns. And, its thermal stability was observed at about 507 K. Second, from the NMR experimental results, the ^1H chemical shifts in NH_3 and the influence of C1 located close to NH_3 near T_C are large, which implies that the structural change of $CuCl_4$ linked to the N–H···Cl is large. On the other hand, the ^1H $T_{1\rho}$ values in NH_3 are shorter than those in CH_2, and the ^{13}C $T_{1\rho}$ values for C1 located close to NH_3 are shorter than the $T_{1\rho}$ values of C2 and C3. The $T_{1\rho}$ value of C1 located close to the paramagnetic Cu^{2+} ion is shorter than the $T_{1\rho}$ values of C2 and C3 located far from Cu^{2+} because of the

magnetic moment of the paramagnetic ion. Consequently, the main contribution to the phase transition was the structural change of the N–H···Cl hydrogen bond and was associated with the reorientational dynamics of the $CuCl_4$ anion. The role on N–H···Cl hydrogen bond in this study will be helpful of hybrid perovskite types for their applications in fuel cell and solar cell.

Author contributions

A. R. Lim performed NMR experiments and wrote the manuscript. M. Y. Choi and S. J. Lee measured TGA and DSC experiments. H. Ju performed XRD experiment.

Conflicts of interest

There are no conflicts to declare.

Acknowledgements

References

1 C. N. R. Rao, A. K. Cheetham and A. Thirumurugan, *J. Phys.: Condens. Matter*, 2008, **20**, 83202.

2 Z. Cheng and J. Lin, *CrystEngCom*, 2010, **12**, 2646.

3 M. F. Mostafa and S. S. El-khiyami, *J. Solid State Chem.*, 2014, **209**, 82.

4 S. Gonzalez-Carrero, R. E. Galian and J. Perez-Prieto, *Part. Part. Syst. Charact.*, 2015, **32**, 709.

5 S. K. Abdel-Aal, G. Kocher-Oberlehner, A. Ionov and R. N. Mozhchil, *Appl. Phys. A*, 2017, **123**, 531.

6 W. Liu, J. Xing, J. Zhao, X. Wen, K. Wang, L. Peixiang and Q. Xiong, *Adv. Opt. Mater.*, 2017, **5**, 1601045.

7 P. Mondal, S. K. Abdel-Aal, D. Das and S. K. Manirul Islam, *Catal. Lett.*, 2017.

8 M. Elseman, A. E. Shalan, S. Sajid, M. M. Rashad, A. M. Hassan and M. Li, *ACS Appl. Mater. Interfaces*, 2018, **10**, 11699.

9 J. A. Aramburu, P. Garcia-Fernandez, N. R. Mathiesen and J. M. Garcia-Lastra, *J. Phys. Chem. C*, 2018, **122**, 5071.

10 K. Pradeesh, G. S. Yadav, M. Singh and G. Vijaya Prakash, *Mater. Chem. Phys.*, 2010, **124**, 44.

11 S. Saikumar, J. J. Ahmad, G. Baumberg and G. Vijaya Prakash, *Scr. Mater.*, 2012, **67**, 834.

12 B. Staskiewicz, O. Czupinski and Z. Czapla, *J. Mol. Struct.*, 2014, **1074**, 723.

13 S. Ahmad, C. Hanmandlu, P. K. Kanaujia and G. Vijaya Prakash, *Opt. Mater. Express*, 2014, **4**, 1313.

14 Z. Czapla, J. Przeslawski, M. Crofton, J. Janczak, O. Czupinski, A. Ingram and M. Kostrzewa, *Phase Transitions*, 2017, **90**, 637.

15 W. Zang and R.-G. Xiong, *Chem. Rev.*, 2012, **112**, 1163.

16 A. R. Lim and L. K. Kwac, *Sci. Rep.*, 2022, **12**, 8769.

17 S. K. Abdel-Aal and A. Ouasri, *J. Mol. Struct.*, 2022, **1251**, 131997.

18 S. K. Abdel-Aal, M. F. Kandeel, A. F. El-Sherif and A. S. Abdel-Rahman, *Phys. Status Solidi A*, 2021, **218**, 2100036.

19 S. K. Abdel, A. S. Abdel-Rahman, W. M. Gamal, M. Abdel-Kader, H. S. Ayoub, A. F. El-Sherif, M. F. Kandeel, S. Bozhko, E. E. Yakimov and E. B. Yakimov, *Acta Crystallogr., Sect. B: Struct. Sci., Cryst. Eng. Mater.*, 2019, **75**, 880.

20 R. Kind, S. Plesko, P. Gunter, J. Roos and J. Fousek, *Phys. Rev. B: Condens. Matter Mater. Phys.*, 1981, **23**, 5301.

21 M. F. Mostafa, S. S. El-Khiyami and S. K. Alal, *J. Phys. Chem. Solids*, 2018, **118**, 6.

22 M. F. Mostafa, S. S. El-Khiyami and S. K. Alal, *Mater. Chem. Phys.*, 2017, **199**, 454.

23 K. Ahmad and S. M. Mobin, *Energy Technol.*, 2020, **8**, 1901185.

24 S. K. Abdel-Aal and A. Ouasri, *J. Mol. Struct.*, 2022, **1251**, 131997.

25 A. Jaffe, Y. Lin, W. L. Mao and H. I. Karunadasa, *J. Am. Chem. Soc.*, 2015, **137**, 1673.

26 A. Kallel, J. Fail, H. Fuess and A. Daoud, *Acta Crystallogr., Sect. B: Struct. Crystallogr. Cryst. Chem.*, 1980, **36**, 2788.

27 W. T. A. Harrison, *Acta Crystallogr., Sect. E: Struct. Rep. Online*, 2005, **61**, m1951.

28 M. F. Mostafa and A. Hassen, *Phase Transitions*, 2006, **79**, 305.

29 P. A. N. Xiao-Wei, W. U. Gang, W. A. N. G. Mang and C. H. E. N. Hong-Zheng, *J. Zhejiang Univ., Sci., A*, 2009, **10**, 710.

30 Q. Chen, N. D. Marco, Y. Yang, T.-B. Song, C.-C. Chen, H. Zhao, Z. Hong, H. Zhou and Y. Yang, *Nano Today*, 2015, **10**, 355.

31 I. M. Hermes, S. A. Bretschneider, V. W. Bergmann, D. Li, A. Klasen, J. Mars, W. Tremel, F. Laquai, H.-J. Butt, M. Mezger, R. Berger, B. J. Rodriguez and S. A. L. Weber, *J. Phys. Chem. C*, 2016, **120**, 5724.

32 S. K. Abdel-Aal, A. S. Abdel-Rahman, G. G. Kocher-Oberlehner, A. Ionov and R. Mozhchil, *Acta Crystallogr., Sect. A: Found. Adv.*, 2017, **70**, C1116.

33 E. Strelcov, Q. Dong, T. Li, J. Chae, Y. Shao, Y. Deng, A. Gruverman, J. Huang and A. Centrone, *Sci. Adv.*, 2017, **3**, e1602165.

34 Y. Liu, L. Collins, R. Proksch, S. Kim, B. R. Watson, B. Doughty, T. R. Calhoun, M. Ahmadi, A. V. Ievlev, S. Jesse, S. T. Retterer, A. Belianinov, K. Xiao, J. Huang, B. G. Sumpter, S. V. Kalinin, B. Hu and O. S. Ovchinnikova, *Nat. Mater.*, 2018, **17**, 1013.

35 J. Lee, W. Lee, K. Kang, T. Lee and S. K. Lee, *Chem. Mater.*, 2021, **33**, 370.

36 A. R. Lim, *Sci. Rep.*, 2020, **10**, 20853.

37 A. R. Lim, S. H. Kim and Y. L. Joo, *Sci. Rep.*, 2021, **11**, 8408.

38 X. Guan and R. E. Stark, *Solid State Nucl. Magn. Reson.*, 2010, **38**, 74.

39 A. Abragam, *The Principles of Nuclear Magnetism*, Oxford University press, 1961.

40 R. K. Harris, *Nuclear Magnetic Resonance Spectroscopy*, Pitman Pub., UK, 1983.

41 J. L. Koenig, *Spectroscopy of Polymers*, Elsevier, New York, 1999.